Microscale mechanism of tailing thickening in metal mines

Huazhe Jiao, Wenbo Yang, Zhu'en Ruan, Jianxin Yu, Juanhong Liu, and Yixuan Yang

View the article online at SpringerLink or IJMMM Webpage.

Articles you may be interested in

Bao-hua Yang, Ai-xiang Wu, Guillermo A. Narsilio, Xiu-xiu Miao, and Shu-yue Wu, Use of high-resolution X-ray computed tomography and 3D image analysis to quantify mineral dissemination and pore space in oxide copper ore particles, *Int. J. Miner. Metall. Mater.*, 24(2017), No. 9, pp. 965-973. https://doi.org/10.1007/s12613-017-1484-4

Hao-bin Zhu, Wen-long Zhan, Zhi-jun He, Ying-chang Yu, Qing-hai Pang, and Jun-hong Zhang, Pore structure evolution during the coke graphitization process in a blast furnace, *Int. J. Miner. Metall. Mater.*, 27(2020), No. 9, pp. 1226-1233. https://doi.org/10.1007/s12613-019-1927-1

Xiao-guang Liu, Yan Li, Wen-dong Xue, Jia-lin Sun, and Qian Tang, Shear-thickening behavior of Fe-ZSM5 zeolite slurry and its removal with alumina/boehmites, *Int. J. Miner. Metall. Mater.*, 25(2018), No. 6, pp. 682-688. https://doi.org/10.1007/s12613-018-1615-6

Yong Wang, Ai-xiang Wu, Zhu-en Ruan, Zhi-hui Wang, Zong-su Wei, Gang-feng Yang, and Yi-ming Wang, Reconstructed rheometer for direct monitoring of dewatering performance and torque in tailings thickening process, *Int. J. Miner. Metall. Mater.*, 27(2020), No. 11, pp. 1430-1437. https://doi.org/10.1007/s12613-020-2116-y

Qian Zhou, Juan-hong Liu, Ai-xiang Wu, and Hong-jiang Wang, Early-age strength property improvement and stability analysis of unclassified tailing paste backfill materials, *Int. J. Miner. Metall. Mater.*, 27(2020), No. 9, pp. 1191-1202. https://doi.org/10.1007/s12613-020-1977-4

Xue-qiu He, Chao Zhou, Da-zhao Song, Zhen-lei Li, An-ye Cao, Shen-quan He, and Majid Khan, Mechanism and monitoring and early warning technology for rockburst in coal mines, *Int. J. Miner. Metall. Mater.*, 28(2021), No. 7, pp. 1097-1111. https://doi.org/10.1007/s12613-021-2267-5

IJMMM WeChat   QQ author group

Microscale mechanism of tailing thickening in metal mines

Huazhe Jiao[1,2], *Wenbo Yang*[1], *Zhu'en Ruan*[2],✉, *Jianxin Yu*[1], *Juanhong Liu*[2], *and Yixuan Yang*[1]

1) School of Civil Engineering, Henan Polytechnic University, Jiaozuo 454000, China

2) School of Civil and Resource Engineering, University of Science and Technology Beijing, Beijing 100083, China

Abstract: Water-locking flocs formed by ultrafine tailings particles will damage the thickener underflow concentration in the thickening process during paste preparation. The relationship between the mesostructure and seepage characteristics of tail mortar is typically ignored when investigating the deep dehydration stage. A shearing seepage test of an unclassified tailing–sedimentation bed was performed with copper tailings, and the morphology and geometric distribution of micropores were analyzed via X-ray computed tomography. Moreover, the shearing evolution of the micropore structure and seepage channel was investigated to evaluate the dewatering performance of underflow slurry using a three-dimensional reconstruction approach. The results show that porosity decreases considerably under shearing. The connected-pore ratio and the average radius of the throat channel reach peak values of 0.79 and 31.38 μm, respectively, when shearing is applied for 10 min. However, the reverse seepage velocity and absolute permeability in the bed decrease to various extents after shearing. Meanwhile, the maximum flow rate reaches 1.537 μm/s and the absolute permeability increases by 14.16%. Shearing alters the formation process and the pore structure of the seepage channel. Isolated pores connect to the surrounding flocs to form branch channels, which then become the main seepage channel and create the dominant water-seepage flow channel.

Keywords: paste thickening; computed X-ray tomography; shear action; pore structure; seepage channel

1. Introduction

Mining plays an essential role in the national economy, but tailings from mineral processing plants cause serious environmental pollution and dam failure-related risks to society [1–3]. The utilization of metal solid waste from mines is crucial in realizing the sustainable development of a green ecology as well as carbon neutrality. Cemented paste backfill (CPB) mining technology is a crucial branch of underground mining methods that can efficiently reuse the tailing waste and provide adequate support to an underground goaf [4–5].

However, the particle size of the tailing discharged from plants decreases [6–7] in the development of beneficiation technology. Fine particles pose a serious challenge to gravity dewatering and thickening operations. Slurry segregation and pipeline blockage occur during transportation once the thickener produces a low-concentration underflow because paste materials cannot be prepared. Slurry bleeding in the underground stope causes cement loss and mechanical strength reduction, thereby decreasing the support for the surrounding rock as well as for equipment operation.

The tailing thickening process has been extensively investigated in past decades to improve the underflow of thickeners used with CPB technology. However, there is a lack of an effective dewatering process because of the micropore structure and the unverified evolution of the seepage channel inside the tailing deposition bed. Several studies have been conducted on the following aspects.

First, Philip *et al.* [8] demonstrated that the continuous thickening process is a high-efficiency dewatering operation in the field plant in terms of thickener underflow concentration improvement. Nasser *et al.* [9] showed that the floc size decreases and the density increases when the number of surface particle ions increases from 10% to 35%, which benefits the floc settling velocity and underflow concentration. Wu *et al.* [10] performed pilot-scale tests to improve the thickener performance according to the interaction between colloidal particles subject to different temperatures and mixing conditions. Winterwerp *et al.* [11] described field and laboratory measurements of floc size and settling velocity of cohesive sediment in an estuarine environment and its modelling. The measurements and modelling showed a considerable variation in floc size, hence settling velocity over the tide and over the spring-neap tide cycle. Yang *et al.* [12] explored the flocculation evolution and revealed that appropriate shearing can improve the collision efficiency and hydrophobic flocculation as well as reshape the tailing floc arrangement, thereby improving the dewatering process.

Second, tailing bed shearing–dewatering has attracted considerable research interest. Wang *et al.* [13] performed continuous thickening tests using a semi-industrial device and determined the concentration distribution law of the tailing bed. However, the dynamic relationship of solid–liquid separation in tailing dewatering requires further investiga-

Springer

tion. Jiao *et al.* [14] investigated the evolution of the pore structure and throat before and after shearing by using a pore network model (PNM). Qin *et al.* [15] examined the modification of the network structure of tailing flocs under shearing and its effect on sediment consolidation.

Third, reverse seepage in the tailing deposition bed plays a crucial role in the dewatering process. Wang *et al.* [16] suggested that the static compression of the bed mainly depends on gravity, particles are compact in dynamic compression, and the channel created by rake pickets in the bed allows the trapped water to move upward. Ma *et al.* [17–18] established a one-dimensional three-phase radial water–rock–mud flow model to investigate the fault rock during sudden water inrush as well as mud water features and three-phase flow in the model of the continuity equation. They also described rock particle migration and the momentum conservation of three-phase fluid migration with the filling constitutive disinvestment equation and the non-Darcy flow equation. These parameters in variable size distribution and water pressure were obtained from the one-dimensional radial seepage test and one-dimensional radial particle migration using the porosity and permeability of water features. The porosity and permeability of the water inflow process could be divided into four stages: rapid increase, slow increase and decrease, slow climb, and stabilization. Zhang *et al.* [19] demonstrated that demineralization can increase the porosity and permeability of coal slurry and reach a seepage threshold, at which the permeability changes rapidly.

Studies on the flocculation and settlement process of unclassified tailing slurry fail to explain the mode of trapped-water discharge from the floc structure and the need to further deepen the relationship between the quantitative characterization of microstructures and thickening performances. Topological analysis of the three-dimensional characteristics and pores of the floc network is impossible, and the reverse seepage process and mechanism remain unknown. Meanwhile, a method for quantitatively analyzing the temporal and spatial characteristics of the formation, distribution, disappearance, and connectivity of the seepage flow channel remains lacking.

Therefore, the characteristics and evolution of the micropore structure in tailing slurry were explored using high-precision microtomography, and changes in the porosity, pore size distribution, pore connectivity, and other parameters were observed with a three-dimensional image analysis method. The influence of a single-phase water-seepage channel and the accompanying shear evolution on the dewatering performance of underflow slurry is simulated by solving the absolute permeability. Finally, the blocking process of the water channel is quantitatively analyzed to reveal the thickening and dewatering mechanism of the underflow slurry.

2. Experimental

2.1. Unclassified tailing–thickening test

Fig. 1 shows the particle size distribution of tailings. The

average particle size is <0.03 mm; >50% of the particles are smaller than 0.019 mm, <30% are smaller than 0.037 mm, and 10% are larger than 0.074 mm.
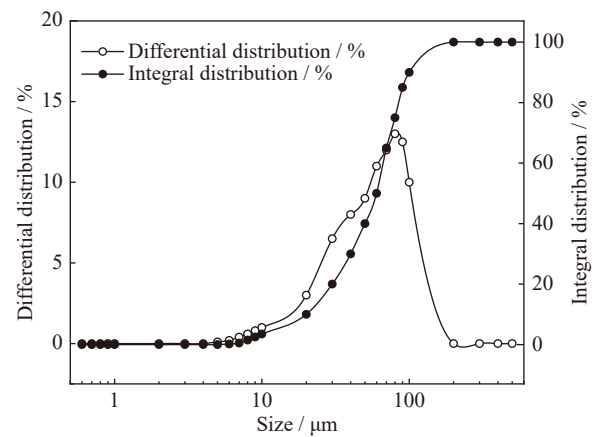

Fig. 1.   Particle size distribution of unclassified tailings.

The pilot scale of a continuous thickener with a continuous feed well was used to simulate the field thickener operation. Specific parameters are listed in Table S1.

The tailing slurry and flocculant dilution were pumped into the thickener feed well to form settling flocs. Tailing flocs were deposited at the bottom of the thickener. The tailing bed specimen was sampled for 30 min when the bed height reached 10 cm. The above steps were restarted for each sample because the settling column had to be removed during sampling. Shearing was introduced after obtaining the first sample; the bed height reached a maximum of 20 cm; and the stirring times were 10, 30, and 60 min for the second, third, and fourth sampling instances, respectively. The process is shown in Fig. S1.

The feed slurry at a concentration of 15wt% was diluted to 5wt% before being pumped into the feed well to mix with the flocculant at a dosage of 20 g/t. The solid-feed flux, residence time, bed height, and rake rotation were 0.2 $h^{-1} \cdot m^{-2}$, 3 h, 20 cm, and 0.2 r/min, respectively.

2.2. Permeability test device

The permeability coefficient is defined as the unit flow under a unit hydraulic gradient that represents the difficulty of a fluid flowing through the porous structure [20–21]. The permeability coefficient is an index for evaluating the compactness and pore distribution of media. Permeability is affected by several factors, such as porosity, pore ratio, size, number, and pore connectivity [22].

The constant head permeability test was adopted according to the ASTM E1417 liquid-penetration test standard to calculate the outlet water permeability coefficient [23–24]. Fig. S2 shows the test device.

2.3. Permeability test method

Feeding was stopped after the shear thickening test, and the test was changed to the reverse seepage procedure to perform the constant head permeability test, as shown in Fig. S3. The appropriate flow rate was then optimized to ensure the

occurrence of reverse seepage without turbid overflow. The settling column was filled with the slurry to the cross-section at height L with an area A; the valve was opened, and water flowed through the sample from bottom to top and was discharged as the overflow. The water volume V flowing through the slurry was measured within a specific time t after the head difference H and overflow Q were stable.

The flow rate of the filtrate is tested through the experiment; i.e., the volume of outflow water per unit time and the appropriate flow rate are determined. The water valve should be opened to allow the water to flow through the sample from bottom to top and discharge from the overflow port, as the area of the injection pool is large and the filling interface in the settling column is small. During this time, the height of the water in the injection pool should remain unchanged. Therefore, the water should be injected irregularly to ensure the stability of the water flow, overflow, and head height.

2.4. CT scanning process

The CT scanning process is presented as follows: (1) Per-form continuous thickening experiments with and without shear. (2) Disassemble the target bed height, underflow concentration, and residence time, followed by the settling column. Discharge the supernatant to expose the target detection bed. (3) Slowly insert the sampling tube with a diameter and height of 20 mm and 100 mm, respectively. Remove the lowest settling column to detect the resident slurry inside the line. (4) Insert a double plastic plate into both ends of the tube to seal the slurry. Perform the test four times under various conditions and then label the four specimens S1, S2, S3, and S4, as shown in Fig. 2.

Transverse (1800) and longitudinal (1350) slices were obtained from each specimen after scanning. The resolution ratio of each image is 1395 pixel × 1452 pixel. Only a part (red area in Fig. 2) was analyzed using Avizo software. The analysis area remained unaffected by the disturbance caused by sampling and scanning because the four sides of this region were far from the sampling tube wall. Images were processed using ImageJ software in preparation for 3D reconstruction. Fig. S4 presents the 3D reconstruction process.
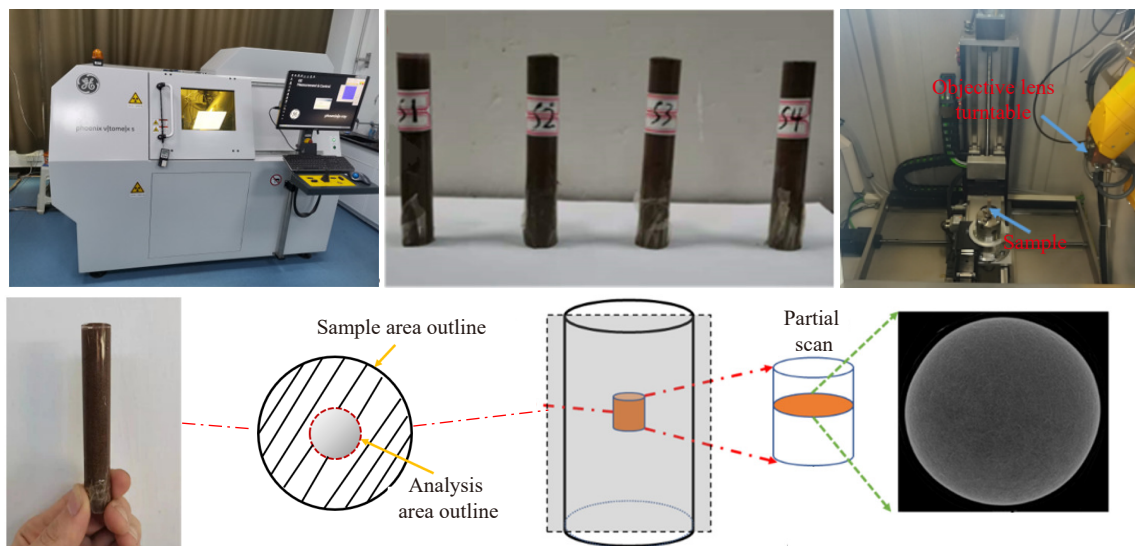

Fig. 2.   High-precision industrial computed tomography.

3. Results

3.1. Experimental results

The results were obtained from an average of five data points to ensure the accuracy of the measured permeability coefficient. The test process and results are listed in Table 1. As shown in Table 1, the underflow concentration under various rake speeds and resident times in the thickener was 45.3vol%, 47.8vol%, 56.4vol%, and 58.7vol%. The adoption of rake shearing improved the underflow concentration. After 60 min of shearing, the underflow concentration increased by 13.4vol% compared with the control specimen. The tailing bed porosity was substantially reduced with rake shearing and resident time.

Table 1.   Calculation of slurry seepage test results

Specimen	Factors				Results		
	Rake shearing time / min	Hydraulic head / cm	Inflow / (cm^3·s^{-1})	Bed height / cm	Concentration / vol%	Seepage velocity / (10^{-5} cm·s^{-1})	Permeability coefficient / (10^{-5} cm·s^{-1})
S1	0	10	0.02	10	45.3	2.68	1.73
S2	10	15	0.02	10	47.8	2.51	1.57
S3	30	25	0.02	10	56.4	2.27	1.24
S4	60	30	0.02	10	58.7	1.83	1.06

3.2. Porosity and pore distribution

Using the Avizo data visualization, analysis and modeling system, we can see the three-dimensional spatial structure distribution of the morphological characteristics of the tailing bed microstructure [25].
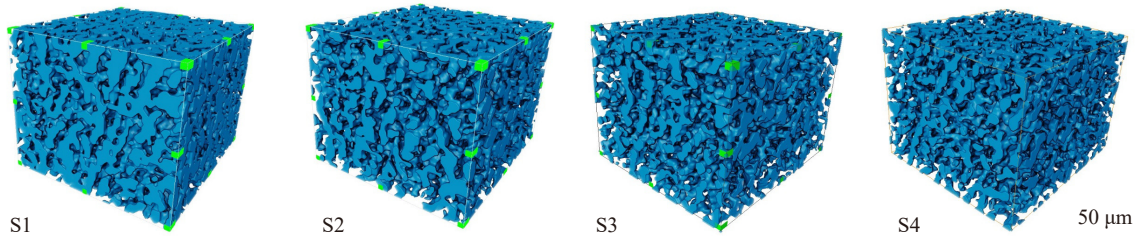
Porosity is defined as the ratio of the pore volume to the total volume in a 3D reconstruction model [26–27]. The blue solid mass in Fig. 3 represents the pore space.

Fig. 3.   **Evolution process of the pore structure during shearing.**

The fragmented pore structure evolution from S1 to S4 was due to continuous rake shearing. The pore space was filled by trapped water in the control specimen. Cracked pores indicate that the water is discharged upward and that the shearing process contains a high solid concentration.

As shown in Fig. 4, the porosity of specimen S1 (control specimen) is 49.94% without shearing. After shearing is adopted, the porosity decreases to 27.66% in a nonlinear relationship with shearing time.
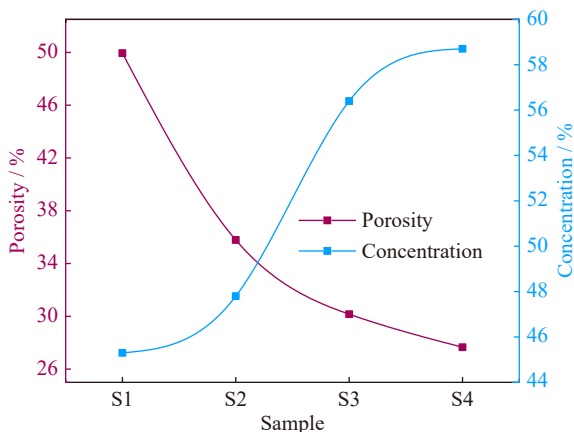

Fig. 4.   **Relationship between porosity and the concentration distribution.**

When the control specimen and specimen S2 was subject to shearing for 10 min, the concentration increases only slightly. However, Fig. 4 illustrates that the pore structure undergoes reorganization–breakage–reorganization in this short, crucial period under shearing. Closed pores open, isolated pores connect with the surrounding space, and isolated pores are rearranged before the trapped water is discharged.

Specimens S2 to S3 were subjected to a 20-min shearing time. Fig. 4 shows a sharp decrease in porosity because the seepage flow channel is formed because of the ongoing rearrangement of pore groups during this period. Consequently, the trapped water at the bottom of the tailing bed seeps upward along the track, thus increasing the underflow concentration.

Shearing of specimens S2 and S3 demonstrated that the porosity decreases to a steady value. The flow channel closes after the water discharge is stopped, and the seepage pressure in the bed is balanced after 60 min of rake shearing in the case of specimen S4. The continuous rake shearing and additional pressure are necessary conditions for a future increase in underflow concentration.

Fig. 5 shows the three-dimensional pore volume distribution. The specimen gradually changes from a loose state to a dense state, the number of large-volume pores slowly increases, and the number of small-volume pores decreases as shearing progresses. Pores smaller than 50 mm^3 account for 40.66% of the total volume of specimen S1 without shearing. Pores larger than 3000 mm^3 account for 14.91%, exhibiting a considerable variation in pore volume distribution. Pores smaller than 50 mm^3 and larger than 3000 mm^3 in specimen S4 after shearing account for 21.37% and 28.49%, respectively, of the total volume of specimen S4. The pore volume distribution is uniform.

Tailing flocs are displaced under the original loose arrangement and rearranged under the action of gravity and tailing bed pressure due to the shearing. Flocs are deformed and compacted to form a high-concentration underflow. The original macropores are squeezed, twisted, and divided to create numerous micropores, leading to an increase in the number of pores but a decrease in the total porosity.

3.3. Analysis of the connected pore structure

3.3.1. Equivalent pore network model

The PNM refers to a stick framework comprising spheres and stick bodies. The pores and throats are characterized and observed using a geometric model, in which a sphere and a tube bundle represent the pore and the throat, respectively [28–30]. The volume of the sphere is similar to that of the pore at the corresponding function, and the size and position of the sphere and tube bundle reflect the size of the pore and throat, respectively [31]. The PNM can perform a statistical analysis to realize a quantitative description of pore distribution characteristics while intuitively expressing the distribution characteristics of the pore throat [32–33].

3.3.2. Pore structure quantitative analysis

The PNM is extracted from the three-dimensional reconstruction results of four specimens, as shown in Fig. 6. Para-
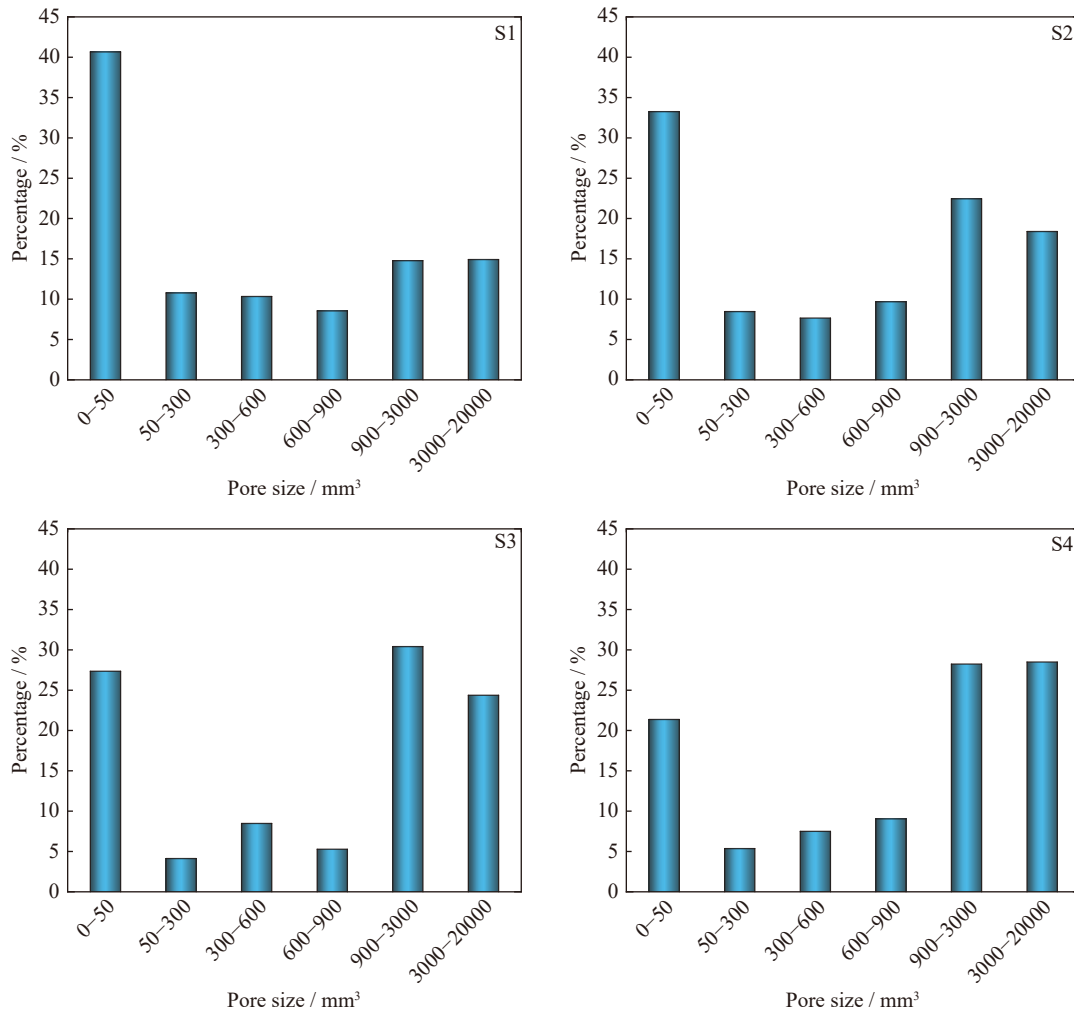
Fig. 5.   Three-dimensional pore volume distribution.

meters such as sphere/stick radius and coordination number are listed in Table S2.

As shown in Fig. 7, the average coordination number of the spheres in specimens S1, S2, S3, and S4 is 10.82, 11.06, 9.15, and 7.38, respectively. The coordination number decreases by 31.79%, and the pore connectivity is reduced considerably after shearing. The pore coordination number of specimen S2 reaches the maximum at 29.87% in the range of 10–15 during shearing. The static balance formed by flocs is broken by shearing, and pores gather into water diversion channels with enhanced pore connectivity during the initial stage of the shearing.

The pore coordination number gradually decreases due to shearing. The reduction of the coordination number between pores due to the shear force indicated that shearing can alter the transformation of pore distribution and benefit the discharge of water trapped in flocs because of the reduced connection between pore structures.

Fig. 7 presents the change in sphere size during the shear process of unclassified tailing slurry. The pore distributions in the bed slurry are uneven. The two types of pores facilitate pore size and evolution analysis. The equivalent radius of small and large spheres is <40 and >80 μm, respectively.

The average radius of the sphere is 76.79 μm. The average radius of the sphere of specimens S2, S3, and S4 is 73.21, 68.65, and 66.36 μm, with a shearing time of 10, 30, and 60 min, respectively. The average sphere radius decreases gradually with shearing. The number of delicate spheres with equivalent diameters ranging from 20 to 40 μm reaches 26.87%, which is the peak value after 60 min of shearing,
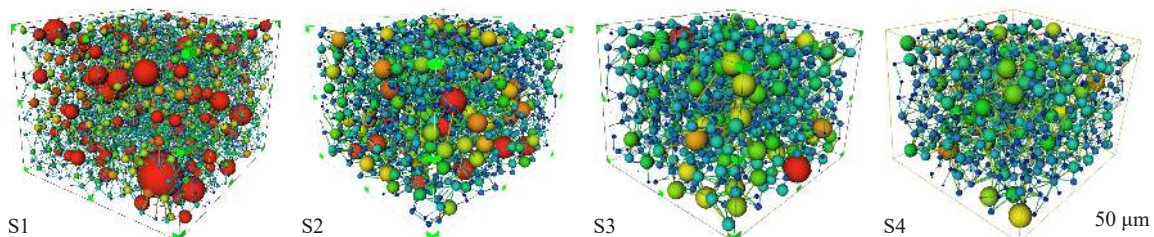

Fig. 6.   PNM evolution in the shear process.
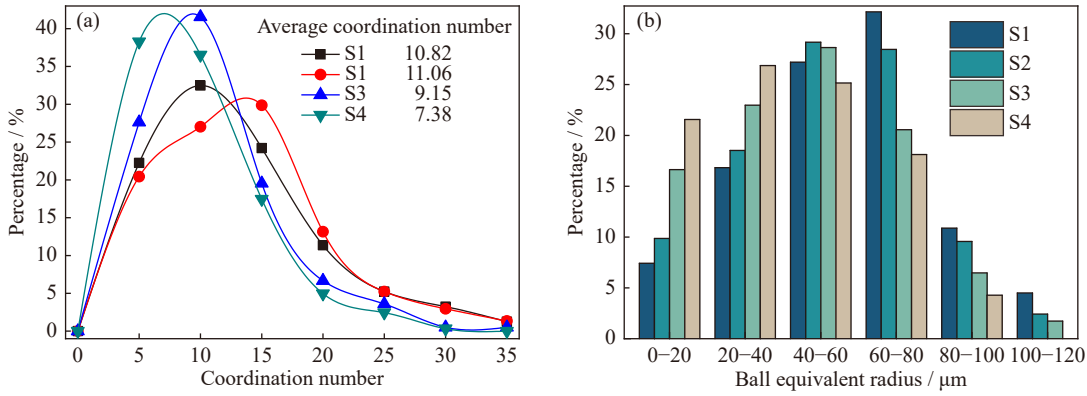
Fig. 7.   Parameter statistics of pore network model: (a) pore coordination number; (b) sphere radius size.

while the number of pores with a diameter of 60–80 μm decreases sharply.

The results indicate that the pore size distribution is uniform, the floc structure in the bed is compact, and a large amount of trapped water is discharged. The number of large spheres decreases, and the proportion of small spheres increases with shear time. This finding demonstrates that shearing will break a large ball into several small spheres, and the water trapped in the pores will be discharged from the bed.

4. Discussion

4.1. Formation and distribution of the seepage flow channel during thickening

Figs. S5 and S6 show the floc compression state and water-seepage flow channel during the thickening process, respectively. The floc spacing is large, and the pores and floc network structure form a static equilibrium state in the S1 stage. The water channel develops with the progress of shearing at 10 min. The track is formed first and then closes with the shearing time. The increased density of particles and reduced number and size of water channels increase the bed concentration.

The saturated fluid flow in porous media is investigated under the assumption that pores and their radii adhere to fractal distribution [34–35]. According to the generalized Hagen–Poiseuille equation, the flow through a unit volume is expressed as

$$q = nA \frac{\pi}{8} \frac{\Delta P}{L_e} \frac{\bar{r}^4}{\mu} \tag{1}$$

where q is the flow through a single pipe, cm^3/s; n is the number of tubes per unit scope; A is the area of the section, mm^2; L_e is the length of a curved line; $\bar{r}$ is the average value of the hydraulic radius of a single pipe, mm; μ is the viscosity coefficient of the fluid, MPa/s; ΔP is the pressure, MPa.

According to Darcy's law,

$$q = \frac{KA\Delta P}{\mu L} \tag{2}$$

$$\emptyset = \frac{nA\pi\bar{r}^2 L_e}{AL} \tag{3}$$

where K is the permeability, m^2; L is the seepage length, m; porosity $\emptyset$ is the ratio of the pore volume to the porous track.

Seepage in the slurry can also be observed clearly at the microscale. Therefore, analyzing the pore channel at the microscale is necessary to visualize the bed dehydration channel in the thickening process of unclassified tailing slurry.

The pore channel is extracted to obtain the seepage channel model, as shown in Fig. 8. The small and thick pore volume at the bottom of the sample indicates high concentrations.
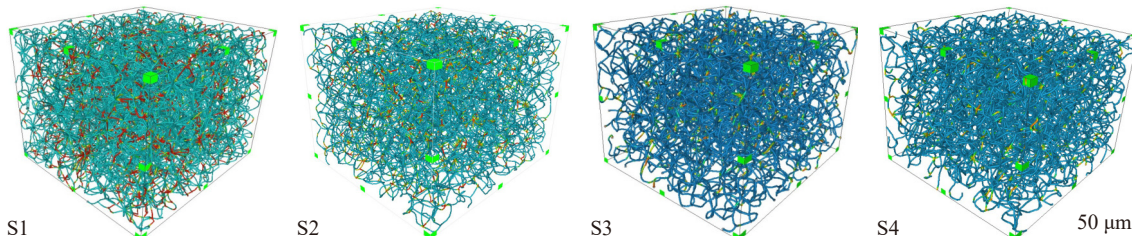

Fig. 8.   Model of the porous seepage channel.

4.2. Water-seepage simulation

4.2.1. Solution of absolute permeability

Absolute permeability refers to the transmission capacity of porous media [36–37]. Darcy's law is used to solve the absolute permeability of incompressible fluids [38]:

$$K = \frac{\mu_P q L}{A (P_{in} - P_{out})} = \frac{\mu_P q L}{A \Delta P} \tag{4}$$

where μ_P is the viscosity of the P-phase fluid, MPa/s; ΔP is the pressure difference between outlet and inlet; P_{in} and P_{out}

are the inlet and outlet pressures, respectively, MPa.

4.2.2. Model input

The XLab module of the Avizo software platform was used for performing a simulation, and pores in the model were used to simulate the absolute permeability. The generation process of the Avizo model is presented as follows. The interactive thresholding module is used to generate the pore model, and then the absolute experiment simulation module is employed to simulate the pore model with a computer graphics processor. The Stokes equation is applied to simulate the fluid flow in a pore, and pure water is used as the flow track. The flow velocity at the outlet boundary is divided, and the water volumetric flow rate is obtained using the tailing model. The model's vertical opposite sides are used as the velocity inlet and pressure outlet boundaries, and the remaining flow boundaries and hole walls are viewed as no-slip walls (the velocity is 0). Using Darcy's law, the Navier–Stokes equation, and the Stokes equation, an absolute permeability calculation model is established, which is used to calculate the internal pore absolute permeability and simulate the seepage situation [39]. The inlet pressure, outlet pressure, and fluid viscosity are 130 kPa, 100 kPa, and 0.001 Pa·s, respectively. The boundary parameter settings are listed in Table S3. Note that the analyzed volumes are cropped from the original geometry. Output files from the raw geometry are infeasible because of random access memory limitations in computing devices. The very high flow velocity in the lower cross-section of the pore structure indicates that the openings between the pores are conducive to fluid transport. The velocity distribution in the same channel also presents noticeable differences. The flow velocity reaches the maximum value at the center of the track and gradually decreases from the middle to both sides, thereby exhibiting a parabolic distribution.

Furthermore, the inlet and outlet of the fluid represent the entire plane. Fig. 9 shows that the inlet and outlet converge because a fluid buffer is set in the seepage module of Avizo software, i.e., a voxel-wide area is added to the image surface perpendicular to the mainstream direction. They are designed to produce a stable region of quasistatic pressure, al-
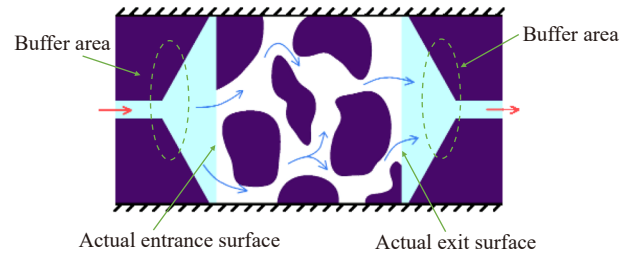

Fig. 9.   Diagram of the single-phase water-seepage simulation.

lowing the fluid to spread freely on the input and output surfaces of the sample.

4.2.3. Simulation results

Figs. 10 and 11, respectively, show that seepage is characterized by streamlined density and color. The flow mainly occurs in the connected pores, leading to an observable dominant flow. The large streamline density represents a large pore-channel diameter. A high flow rate corresponds to a warm color. The seepage rate is fast in the micropores, particularly when the pore channel shrinks. The dewatering flow velocity increases sharply, with the maximum velocity often visible in tiny pores.

As shown in Table S4, the evolution of the seepage channel greatly correlates with slurry thickening and dewatering in the shearing process of 0–60 min. Without shearing, specimen S1 contains a large amount of liquid in the stable state, and the number of pores is sufficient to form a seepage channel. The large-diameter flow channel corresponds to low viscous resistance and high flow velocity, although many secondary water channels exist [40]. The average flow rate in the pore is 1.283 μm/s, the number of streamlines is 489, and the permeability is 13.70×10^{-3} μm^2.

Specimen S2, with a 10-min shearing time, demonstrates that the streamline distribution is thick, the number of streamlines increases by 8.18%. The connected-pore ratio and the average radius of the throat channel reach peak values of 0.79 and 31.38 μm. The reverse seepage velocity and absolute permeability in the bed decrease to various extents after shearing. Meanwhile, the maximum flow rate reaches 1.537 μm/s. The average seepage velocity increases by
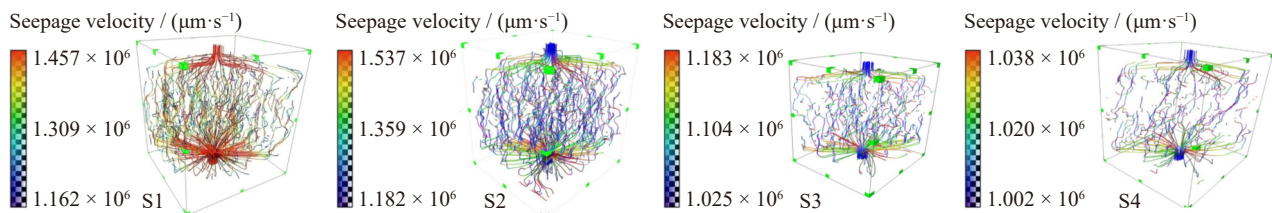

Fig. 10.   Flow channel distributions of the seepage simulation.

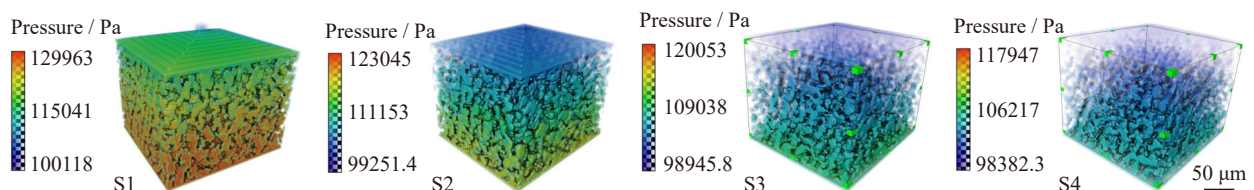

Fig. 11.   Flow pressure distributions of the seepage simulation.

1.48% at 1.302 μm/s, which is higher than that of specimen S1. The porosity decreases from 49.94% to 35.78% after 10 min of shearing. The seepage path is shortened, and the absolute permeability increases by 14.16%, largely due to the accumulation of pores wrapped or separated by flocs. Meanwhile, the secondary water channel converges to the main track, with satisfactory connectivity in the vertical direction, to enhance the dewatering process.

Similarly, the porosity decreases from 35.8% to 27.7% after 30 min of shearing (specimen S3), and the evolution of various parameters positively correlates with porosity. The average seepage velocity of specimen S4, after 60 min of shearing, of only 1.020 μm/s is reduced by 20.50% compared with that of the S1 specimen. The seepage channel diameter is 28.57 μm. The absolute permeability of 9.93×10^{-3} $μm^2$ is reduced by 27.52%. The rake shear directly affects the distribution and connectivity of the flow channel, thereby indicating that shearing benefits thickening performance.

4.3. Seepage flow channel blockage mechanism

The shear evolution process of the seepage flow channel is represented by four stages. Figs. 12 and 13 show the simulation of the particle channel filling process.
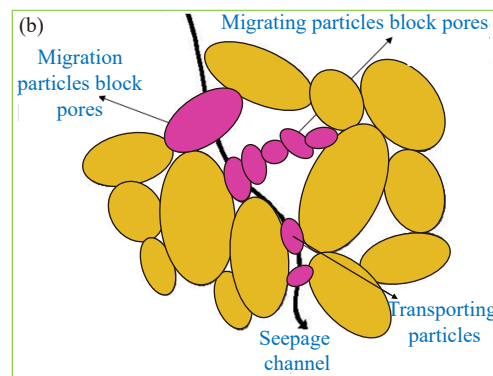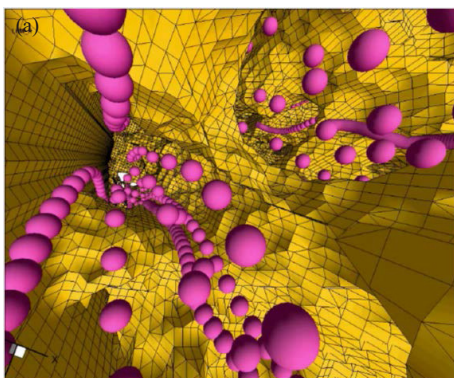
(1) Flow channel formation stage: The floc position and structure are moved by the rake rotation. The water-locking floc structure is destroyed, surrounding fine particles fill the pore structure at the bottom of the bed, and water at the bottom is gradually discharged under the stirring disturbance.

(2) Reverse seepage stage: The sealed water flows upward along the open channel under the action of hydrostatic pressure when the channel is connected. The hydrostatic pressure at the lower part of the slurry decreases, and the floc network structure is reorganized as the water hidden in large pores is discharged. Numerous main channels evolve into secondary and single channels. The main drainage channels are eradicated, and the complete blockage of the pore structure results in the disappearance of porous media and a slow discharge of water.

(3) Pore network reorganization stage: Tailing particles occupy the original water space, the floc network is reorganized, and the channel throat narrows after the water is discharged.

(4) Channel disappearance stage: The rake shear thickens the floc structure, the tracks are blocked by tailings, and the track is annihilated.

Fig. 12. Blocking and migrating particles in pores: (a) fluid path; (b) structural representation.
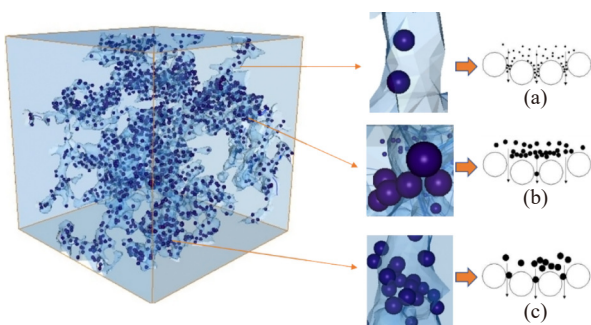

Fig. 13. Simulation diagram of the particle filling channel process: (a) small particles entering the pore throat; (b) medium particles entering the pore throat; (c) large particles entering the pore throat.

5. Conclusions

The preparation of a paste with low-concentration gravity dehydration of full-size metal ore tailings is challenging. Pulping commonly occurs in traditional thickening technology because studies typically focus on the first half of the thickening process, which is the flocculation and settlement process. Notably, the later deep dehydration process is difficult. The permeable performance of the slurry decreases, and a continuous discharge of water to improve the concentration is challenging when the concentration reaches a certain level. The influence of shear action on the concentration and permeability of an ultrafine-grained tailing slurry was explored in this study. CT scanning and three-dimensional reconstruction technology were used to analyze the shear evolution characteristics of pore space structure quantitatively; the dewatering force, path, and mode were clarified. Finally, the following research results were obtained:

(1) The slurry concentration eventually increased by 13.4vol% during the thickening process at the macrolevel compared with specimens without shearing and with 60 min of shearing. The slurry concentration of the bed increased

1546

Int. J. Miner. Metall. Mater., Vol. 30, No. 8, Aug. 2023

continuously with steady shearing. Among the four samples, sample S1 has the maximum permeability coefficient of 13.70×10^{-3} μm^2, and sample S4 has the minimum permeability coefficient of 10.63×10^{-3} μm^2. With the introduction of shearing, the fluidity of the tailing slurry and the permeability coefficient decreased, while the accumulation height and the concentration of bed slurry increased. This finding will greatly improve the preparation of high-concentration paste.

(2) The porosity of the sample decreased considerably at the microlevel when shearing was applied for 10–30 min, indicating that the channel formed at this time is discharged upward and can be considered the main drainage stage. The porosity decreased by 22.28% from 49.94% to 27.66%, and the number of isolated pores first decreased and then increased with the occurrence of shearing time compared with that of samples without shear. Most streamlines are thickly distributed, and secondary channels converge to the main track at the initial stage of shearing. The rake frame changes the formation stage, flocculation, and pore structure of the water guide channel. Isolated pores relate to the surrounding flocs to form branch channels. Multiple branch channels are combined to form the main seepage channel, including the dominant water-seepage flow channel.

(3) The analysis of the blockage mechanism of the seepage channel demonstrated that the flocculation structure is destroyed by shear action, and particles are rearranged, leading to percolation of water and subsequent dehydration under the action of differential pressure. During the whole shear thickening process, particle migration and deposition are dynamic until the maximum displacement is reached. The particle spacing decreases, large pores are broken into tiny pores, the water channel narrows or even closes, and the dehydration and osmosis slow down and eventually cease after the water outflow. Simultaneously, the number of pores increases, the connectivity of pores decreases, and the resulting concentration of slurry increases. Hence, the addition of shear action can effectively dehydrate and settle tailings and increase the underflow concentration.

Acknowledgement

Conflict of Interest

Huazhe Jiao is an editorial board member for this journal and was not involved in the editorial review or the decision to publish this article. The authors declare no potential conflicts of interest.

Supplementary Information

The online version contains supplementary material available at https://doi.org/10.1007/s12613-022-2587-0.

References

[1] M.N. Uugwanga and N.A. Kgabi, Heavy metal pollution index of surface and groundwater from around an abandoned mine site, Klein Aub, *Phys. Chem. Earth Parts A/B/C*, 124(2021), art. No. 103067.

[2] Y. Vasquez, C.M. Neculita, G. Caicedo, *et al.*, Passive multi-unit field-pilot for acid mine drainage remediation: Performance and environmental assessment of post-treatment solid waste, *Chemosphere*, 291(2022), art. No. 133051.

[3] P. Mazumder, A. Das, M. Khwairakpam, and A.S. Kalamdhad, A comprehensive insight into ecological risk assessment and remediation of metal contaminated coal mine soil: Towards a cleaner and sustainable environment, *J. Cleaner Prod.*, 324(2021), art. No. 129185.

[4] A.X. Wu, Z.E. Ruan, and J.D. Wang, Rheological behavior of paste in metal mines, *Int. J. Miner. Metall. Mater.*, 29(2022), No. 4, p. 717.

[5] Q.S. Chen, S.Y. Sun, Y.K. Liu, C.C. Qi, H.B. Zhou, and Q.L. Zhang, Immobilization and leaching characteristics of fluoride from phosphogypsum-based cemented paste backfill, *Int. J. Miner. Metall. Mater.*, 28(2021), No. 9, p. 1440.

[6] H.Z. Jiao, W.L. Chen, A.X. Wu, *et al.*, Flocculated unclassified tailings settling efficiency improvement by particle collision optimization in the feedwell, *Int. J. Miner. Metall. Mater.*, 29(2022), No. 12, p. 2126.

[7] H.Z. Jiao, Y.C. Wu, H. Wang, *et al.*, Micro-scale mechanism of sealed water seepage and thickening from tailings bed in rake shearing thickener, *Miner. Eng.*, 173(2021), art. No. 107043.

[8] P. Ofori, A.V. Nguyen, B. Firth, C. McNally, and M.A. Hampton, The role of surface interaction forces and mixing in enhanced dewatering of coal preparation tailings, *Fuel*, 97(2012), p. 262.

[9] M.S. Nasser and A.E. James, Effect of polyacrylamide polymers on floc size and rheological behaviour of kaolinite suspensions, *Colloids Surf. A*, 301(2007), No. 1-3, p. 311.

[10] Q.S. Chen, L.M. Zhu, Y.M. Wang, J. Chen, and C.C. Qi, The carbon uptake and mechanical property of cemented paste backfill carbonation curing for low concentration of CO_2, *Sci. Total Environ.*, 852(2022), art. No. 158516.

[11] J.C. Winterwerp, A.J. Bale, M.C. Christie, *et al.*, Flocculation and settling velocity of fine sediment, *Proc. Mar. Sci..*, 5(2002), p. 25.

[12] L.H. Yang, H.J. Wang, H. Li, and X. Zhou, Effect of high mixing intensity on rheological properties of cemented paste backfill, *Minerals*, 9(2019), No. 4, art. No. 240.

[13] Z.B. Wang, J. Nan, X.Y. Ji, and Y.M. Yang, Effect of the micro-flocculation stage on the flocculation/sedimentation process: The role of shear rate, *Sci. Total Environ.*, 633(2018), p. 1183.

[14] H.Z. Jiao, S.F. Wang, Y.X. Yang, and X.M. Chen, Water recovery improvement by shearing of gravity-thickened tailings for cemented paste backfill, *J. Cleaner Prod.*, 245(2020), art. No. 118882.

[15] J. H. Qin, J. Zheng, and L. Li, An analytical solution to estimate the settlement of tailings or backfill slurry by considering the sedimentation and consolidation, *Int. J. Min. Sci. Technol.*, 31(2021), No. 3, p. 463.

[16] H.J. Wang, Q.S. Peng, Y. Yang, and J.B. Guo. Research status and prospect of metal tailings thickening technology, *Chin. J. Eng.*, 44(2022), No. 6, p. 971.

[17] D. Ma, H.Y. Duan, J.X. Zhang, X.W. Liu, and Z.H. Li, Numerical simulation of water-silt inrush hazard of fault rock: A three-phase flow model, *Rock Mech. Rock Eng.*, 55(2022), No. 8, p. 5163.

[18] W. Sun, S.Y. Zhang, J.X. Li, and Z.Y. Li, Experimental study

on energy dissipation of layered backfill under impact load, *Constr. Build. Mater.*, 347(2022), art. No. 128478.

[19] G.L. Zhang, P.G. Ranjith, M.S.A. Perera, A. Haque, X. Choi, and K.S.M. Sampath, Characterization of coal porosity and permeability evolution by demineralisation using image processing techniques: A micro-computed tomography study, *J. Nat. Gas Sci. Eng.*, 56(2018), p. 384.

[20] D. Zheng, W.D. Song, Y.Y. Tan, S. Cao, Z.L. Yang, and L.J. Sun, Fractal and microscopic quantitative characterization of unclassified tailings flocs, *Int. J. Miner. Metall. Mater.*, 28(2021), No. 9, p. 1429.

[21] S.Y. Li, C.Y. Qiao, Z.M. Li, and Y.T. Hui, The effect of permeability on supercritical CO_2 diffusion coefficient and determination of diffusive tortuosity of porous media under reservoir conditions, *J. CO_2 Util.*, 28(2018), p. 1.

[22] K.Z. Zhang, S.L. Wang, L. Wang, *et al.*, 3D visualization of tectonic coal microstructure and quantitative characterization on topological connectivity of pore-fracture networks by Micro-CT, *J. Pet. Sci. Eng.*, 208(2022), art. No. 109675.

[23] I. Tretiak and R.A. Smith, A parametric study of segmentation thresholds for X-ray CT porosity characterisation in composite materials, *Composites Part A*, 123(2019), p. 10.

[24] H. Sazegaran and S.M.M. Nezhad, Cell morphology, porosity, microstructure and mechanical properties of porous Fe–C–P alloys, *Int. J. Miner. Metall. Mater.*, 28(2021), No. 2, p. 257.

[25] F.B. Chen, B. Xu, H.Z. Jiao, *et al.*, Triaxial mechanical properties and microstructure visualization of BFRC, *Constr. Build. Mater.*, 278(2021), art. No. 122275.

[26] G. Wang, X.J. Qin, D.Y. Han, and Z.Y. Liu, Study on seepage and deformation characteristics of coal microstructure by 3D reconstruction of CT images at high temperatures, *Int. J. Min. Sci. Technol.*, 31(2021), No. 2, p. 175.

[27] X.M. Ni, J. Miao, R.S. Lv, and X.Y. Lin, Quantitative 3D spatial characterization and flow simulation of coal macropores based on μCT technology, *Fuel*, 200(2017), p. 199.

[28] R. Nemati, J.R. Shahrouzi, and R. Alizadeh, A stochastic approach for predicting tortuosity in porous media via pore network modeling, *Comput. Geotech.*, 120(2020), art. No. 103406.

[29] M. Bankim, V.P.G. Vikram, and T.N.S. Ranjith, An insight into pore-network models of high-temperature heat-treated sandstones using computed tomography, *J. Nat. Gas Sci. Eng.*, 77(2020), art. No. 103227.

[30] S. Babaei, S.C. Seetharam, A. Dizier, G. Steenackers, and B. Craeye, Permeability of cementitious materials using a multiscale pore network model, *Constr. Build. Mater.*, 312(2021), art. No. 125298.

[31] C.Z. Qin, and V.B. Harald, A dynamic pore-network model for spontaneous imbibition in porous media, *Adv. Water Resour.*, 133(2019), art. No. 103420.

[32] J. Yao, W.H. Song, D.Y. Wang, H. Sun, and Y. Li, Multi-scale pore network modelling of fluid mass transfer in nano-micro porous media, *Int. J. Heat Mass Transfer*, 141(2019), p. 156.

[33] M.P.P.C. Santos and M.S. Carvalho, Pore network model for retrograde gas flow in porous media, *J. Pet. Sci. Eng.*, 185(2020), art. No. 106635.

[34] T. Gao, W. Sun, Z. Liu, and H.Y. Cheng, Investigation on fracture characteristics and failure pattern of inclined layered cemented tailings backfill, *Constr. Build. Mater.*, 343(2022), art. No. 128110.

[35] Q.S. Chen, S. Sun, and Y. Wang, *In-situ* remediation of phosphogypsum in a cement-free pathway: Utilization of ground granulated blast furnace slag and NaOH pretreatment, *Chemosphere*, 313(2023), art. No. 137412.

[36] Q.X. Huang, Experimental research of overburden movement and subsurface water seeping in shallow seam mining, *J. Univ. Sci. Technol. Beijing*, 14(2007), No. 6, p. 483.

[37] M.S. Mehdi, O. Pouria, and N. Fatemeh, Salinity of injection water and its impact on oil recovery absolute permeability, residual oil saturation, interfacial tension and capillary pressure, *Egypt. J. Pet*, 26(2017), No. 2, p. 301.

[38] O.B. Rizvandi, X.Y. Miao, and H.L. Frandsen, Fast and stable approximation of laminar and turbulent flows in channels by Darcy's Law, *Alex. Eng. J.*, 60(2021), No. 2, p. 2155.

[39] H.T. Ran, B. Zheng, and Y.Q. Shang, A parallel finite element variational multiscale method for the Navier-Stokes equations with nonlinear slip boundary conditions, *Appl. Numer. Math.*, 168(2021), p. 274.

[40] L. Li, C.D. Ma, S.P. Hu, *et al.*, Effect of the benzene ring of the dispersant on the rheological characteristics of coal-water slurry: Experiments and theoretical calculations, *Int. J. Min. Sci. Technol.*, 31(2021), No. 3, p. 515.